CrossMark

ORIGINAL PAPER

Metamorphic conditions and structural evolution of the Kesebir-Kardamos dome: Rhodope metamorphic complex (Greece-Bulgaria)

Evangelos Moulas[1] · **Filippo Luca Schenker[1,2]** · **Jean-Pierre Burg[1]** ·
Dimitrios Kostopoulos[3]

Abstract The synmetamorphic nappe system of the Rhodope Metamorphic Complex has been deformed into dome-and-basin structures attributed to syn- to post-convergent exhumation. We document the deformation style and present new thermobarometric and geochronological constraints for the Kesebir–Kardamos dome in southern Bulgaria and northern Greece. The dome consists of a migmatitic core overlain by high-grade thrust sheets. Kinematic indicators indicate a continuum from ductile to brittle conditions during exhumation. Thermodynamic modeling applied to the high-grade, intermediate thrust sheets yielded peak conditions of 1.2 GPa and ca 730 °C. New U–Pb SHRIMP-II dating of zircons from rocks of the same unit revealed Late Jurassic–Early Cretaceous (145 Ma) as the time of metamorphic crystallization; some zircon rims yielded Eocene ages (53 and 44 Ma) interpreted as having been thermally reset owing to coeval granitoid magmatism. The high-grade rocks were covered by Lutetian–Priabonian marine sediments after exhumation. Slumps suggest that sedimentation took place in a tectonically active environment. Our new structural, petrological and geochronological results suggest that the major shear zone in the core of the Kesebir-Kardamos dome is equivalent to the Late Jurassic–Early Cretaceous Nestos Shear Zone. Post-Jurassic metamorphic ages recorded in the Rhodope most likely represent crustal rather than deep subduction geodynamic processes.

Introduction

Understanding the geodynamic evolution of a collision zone requires detailed knowledge of the deformation style and the pressure–temperature (*P–T*) conditions of the exposed metamorphic rocks. Furthermore, the chronological relationships between deformation and metamorphism constrain the processes associated with vertical and horizontal movements in the crust. The development of gneiss domes is a first-order indication of upward movements (e.g. Brun 1983) in both compressional and extensional tectonic settings (Burg et al. 2004). The Rhodope metamorphic complex (RMC; Fig. 1; Ricou et al. 1998), in northern Greece and southern Bulgaria, is a synmetamorphic nappe pile that developed during convergence in the Alpine–Himalayan orogenic belt (Burg 2012, and references therein). The nappe system was deformed in dome-and-basin structures during syn- to post-convergent exhumation (Burg et al. 1996). High-pressure rocks showing various degrees of retrogression occur in the intermediate sheets of the nappe system (see Burg 2012 for grouping of units), which contains eclogites (Liati and Mposkos 1990; Liati and Seidel 1996; Moulas et al. 2013; Mposkos et al. 2013) and microdiamond-bearing paragneisses (Mposkos

✉ Evangelos Moulas
evangelos.moulas@erdw.ethz.ch

[1] Department of Earth Sciences, ETH-Zurich, Zurich, Switzerland

[2] Institute of Earth Science, University of Applied Sciences and Arts of Southern Switzerland (SUPSI), Campus Trevano, Manno, Switzerland

[3] Department of Mineralogy and Petrology, National and Kapodistrian University of Athens, Athens, Greece
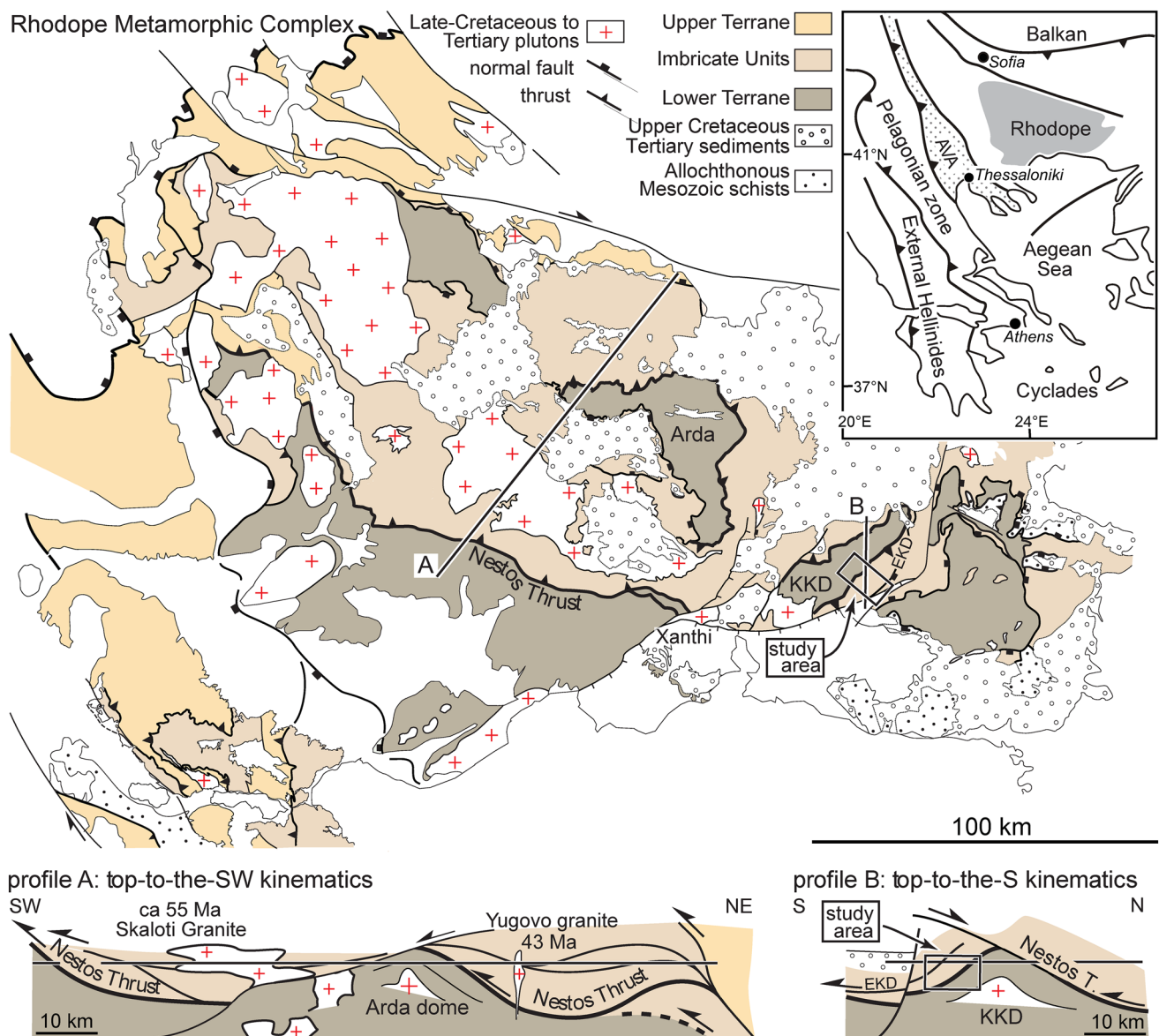
⬢ Springer

Fig. 1 Simplified geological map of the Rhodope Metamorphic Complex (modified after Burg et al. 1996; Bonev 2006; Bonev et al. 2006; Bonev and Beccaletto 2007; Burg 2012). KKD: Kesebir–Kardamos Dome. *EKD* East Kardamos Detachment. *Top right inset* main tectonic units in the Balkan Peninsula. *Box* study area, detailed in Fig. 6. Profiles A and B modified after Burg (2012) and Bonev et al. (2006), respectively

and Kostopoulos 2001; Perraki et al. 2006; Schmidt et al. 2010; Collings et al. 2016). These rocks crop out in the flanks of several, kilometer-wide, gneiss domes such as the Kesebir–Kardamos dome (KKD) in southern Bulgaria and northern Greece (Bonev et al. 2006; Jahn-Awe et al. 2012).

The KKD is an up-arched crustal imbrication that forms an NE–SW trending, sub-elliptic, metamorphic culmination (Fig. 1). In the Bulgarian part of the KKD, the duplication is associated with top-to-the-SW senses of shear recorded by the intermediate thrust units around the dome. Dome-bounding normal shear zones unroofed the migmatitic core

rocks exhumed during an early top-to-the-NE ductile flow (Bonev 2006; Bonev et al. 2006). Thrusting and doming took place during similar amphibolite-facies metamorphic conditions, thus hindering the recognition between compressional and extensional, shallow-dipping faults in the field (Burg 2012). In this work, we investigate the conditions of ductile shearing of the KKD and its relation to the compressional/extensional events in the North Aegean region.

Our new data confirm the spatial continuity in the deformation style of the high-grade rocks in the southeastern

flank of the KKD. Based on structural correlations, *P–T* conditions and absolute ages, we conclude that the peak event for the high-grade metapelites occurred in Jurassic–Cretaceous times, in agreement with published results from central Rhodope (Bosse et al. 2009; Georgieva et al. 2010, 2011; Krenn et al. 2010; Didier et al. 2014). We, therefore, propose that the major thrust zones preserved in the KKD are equivalent to the Late Jurassic–Early Cretaceous Nestos thrust of central Rhodope.

Geological framework and lithotectonic subdivision

The central and eastern Rhodope comprise several tectonometamorphic complexes that are separated by major mylonitic contacts (Burg et al. 1990—Fig. 1). Syn-metamorphic thrusting was responsible for the tectonic juxtaposition of two units with continental affinity. Between these two units, several amphibolite-facies syn-metamorphic imbricates (from the intermediate unit of the RMC) include relics of an earlier high-pressure event (Burg 2012, and references therein). Ophiolitic and magmatic-arc protoliths suggest that these imbricates delineate a suture zone separating the lower Rhodope continental terrane to the south from the European continent to the north (Turpaud and Reischmann 2010; Burg 2012; Froitzheim et al. 2014). In central Rhodope, the Nestos thrust zone is the major segment of this suture zone (Papanikolaou and Panagopoulos 1981; Burg et al. 1990; Nagel et al. 2011). Growing evidence suggests that syn- to post-thickening extension affected the crustal duplex by reworking some of the previous thrust-related contacts (Bonev et al. 2006; Burg 2012) and creating detachment faults (Dinter and Royden 1993; Sokoutis et al. 1993; Brun and Sokoutis 2007).

The KKD has been subdivided into three main units, according to their structural position: a lower, an intermediate and an upper unit (c.f. Bonev et al. 2006). The lower and intermediate units are composed of high-grade metamorphic rocks, whereas the upper unit is composed of sedimentary rocks. The lower and intermediate units of the KKD correspond to the lower and intermediate thrust units of the Rhodope Metamorphic Complex but the uppermost sedimentary unit is not to be confused with the upper metamorphosed terrane of the RMC. Krohe and Mposkos (2002) subdivided the lithotectonic units of the Kesebir–Kardamos dome into two complexes with respect to their relative position to the Kardamos detachment surface (Fig. 1), namely the lower Kardamos complex and the upper Kimi complex. Since, however, the higher parts of the Kardamos complex are lithologically indistinguishable from the Kimi complex (Bonev 2006; Bonev et al. 2006),

we herein follow the simplified discrimination of Bonev et al. (2006) mentioned above.

The lower unit of the KKD is mostly constituted of orthogneisses, representing Permo–Carboniferous metagranitoids (Cornelius 2008); paragneisses, schists and amphibolites occur in small amounts. The orthogneisses show a textural variability being migmatitic, augen, porphyroclastic and equigranular. The intermediate unit (including the Kimi unit in Greece, Figs. 1, 2) is composed of metasediments with pelitic and calc-silicate protoliths, ortho-amphibolites that occasionally show a migmatitic texture, mylonitic orthogneisses and discontinuous marble layers. Amphibolitized eclogite lenses, high-grade metapelites and microdiamond inclusions in garnet and zircon from metapelites have been reported both in the lower and upper parts of this unit (Mposkos and Kostopoulos 2001; Perraki et al. 2006; Cornelius 2008). Large ultramafic bodies, interpreted as dismembered metaophiolite units (Baziotis et al. 2008; Gervilla et al. 2012), are present at the structurally highest levels of the intermediate unit to the east. Estimates of metamorphic conditions vary depending on the structural level where the samples were taken. Metapelites collected near the base of the intermediate unit have recorded *P–T* conditions of 1.0–1.4 GPa and 650–680 °C respectively (Mposkos and Liati 1993), whereas metapelites from higher levels have experienced a high-temperature event at similar pressure (1.1–1.3 GPa and 750–800 °C) subsequently retrogressed to amphibolite facies (0.8–1.0 GPa and 720–740 °C; Bauer et al. 2007).

A Sm-Nd garnet-clinopyroxene-whole-rock age of 119 ± 3.5 Ma from a garnet pyroxenite was ascribed to the high-pressure metamorphic event of the intermediate unit (Wawrzenitz and Mposkos 1997). Similar isotopic ages (109 ± 11 Ma/Sm-Nd; 126 ± 0.7 Ma/Lu-Hf) were obtained also from eclogite samples from the same unit in Bulgaria (Kirchenbaur et al. 2012). In addition, two U–Pb (SHRIMP) zircon ages (117.4 ± 1.9 and 73.5 ± 3.4 Ma) from a garnet-rich mafic rock of the same unit have been interpreted as the times of protolith crystallization and (U) HP metamorphism of the sample, respectively (Liati et al. 2002). Bauer et al. (2007) studied zircons extracted from a metapelite of the intermediate unit and suggested that the (U)HP metamorphic event, responsible for the formation of microdiamonds in metapelites of the intermediate unit, occurred before 170–160 Ma. They, nevertheless, noted that they could not find any microdiamond in the 1800 zircon grains they separated and studied.

Eocene (39–42 Ma) $^{40}Ar/^{39}Ar$ muscovite and biotite ages (Fig. 2) are interpreted as cooling ages below 300–400 °C (Krohe and Mposkos 2002). Clastic, mass-flow sediments lie unconformably on the migmatite units (Caracciolo et al. 2012, and own observations Fig. 3a, b). Slumps in associated turbidites (Fig. 3c, d) witness that the area was
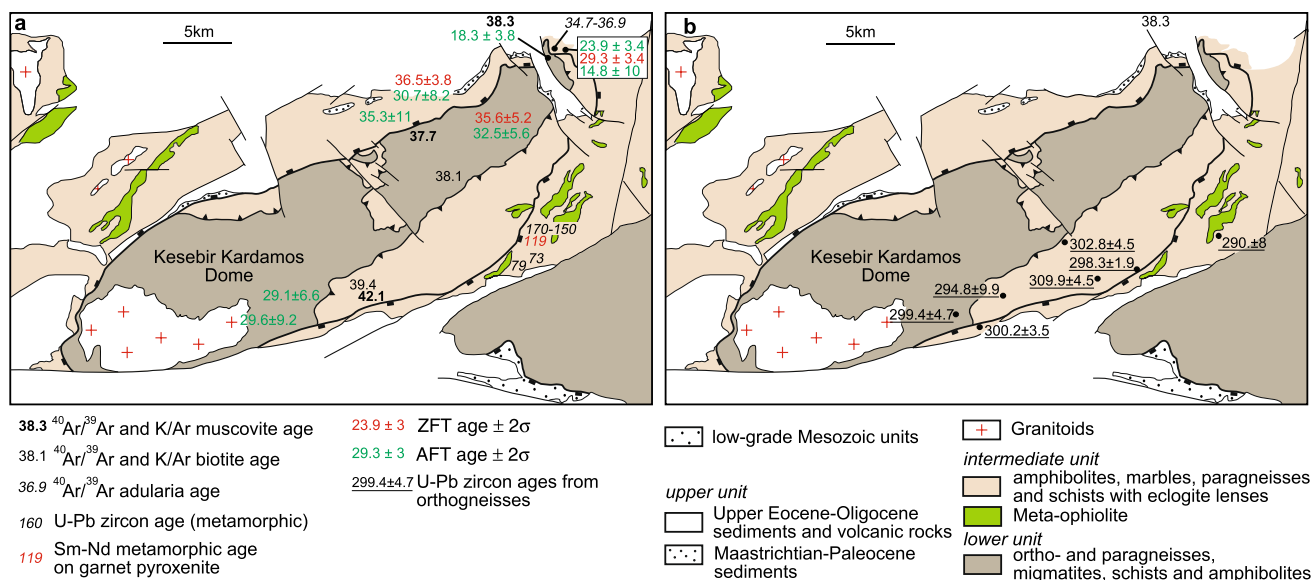
Fig. 2 Simplified geological map (after Burg et al. 1996; Bonev et al. 2006; Sarov et al. 2007) with ages in Ma. **a** Metamorphic and fission-track cooling ages (zircon fission track—ZFT; apatite fission track—AFT; from Wawrzenitz and Mposkos 1997; Krohe and Mposkos 2002; Liati et al. 2002; Marchev et al. 2003, 2004; Bauer et al. 2007; Wüthrich 2009; Márton et al. 2010). **b** Zircon U–Pb ages interpreted as crystallization ages of granitoid protoliths (after Cornelius 2008)

tectonically unstable at the time of sedimentation. The centimetric to decimetric clasts consist of amphibolite, high-grade gneiss and marble suggesting that the source of the detritus was the metamorphic KKD. In the northern part of the KKD, in Bulgaria, the oldest sediments are Maastrichtian–Paleocene (72–56 Ma; Boyanov et al. 1982; Goranov and Atanasov 1992). By contrast, in the Greek part of the dome, the oldest sediments are Lutetian–Priabonian (48–34 Ma; Papadopoulos 1982; Krohe and Mposkos 2002; Caracciolo et al. 2011, 2012). Differences in unconformity age likely represent diachronous transgression on the metamorphic basement.

Deformation pattern and kinematics

On a regional scale, the main foliation is bent and dips outwards following the shape the KKD (Bonev 2006; Bonev et al. 2006). In the Greek part of the dome, it is well-developed, defined by flattened quartz and feldspar and mica-rich layers in quartzo-feldspathic and metapelitic lithologies, respectively, and is dipping gently towards the south, south-east and east (Fig. 4). In such rocks, the lineation is defined by elongated white mica and biotite grains and quartz and feldspar aggregates. In the mafic lithologies, the mineral/stretching lineation is defined by amphiboles.

Generally, in the lower (core) unit of the dome, the lineation is plunging towards the SSW, whereas in the lower part of the allochthonous intermediate unit, lineation is

plunging towards the SE. No abrupt change in foliation and lineation directions has been observed. Mylonites of *S–C* type (Escher et al. 1975; Berthé et al. 1979; Lister and Snoke 1984), fabric asymmetry, rotated clasts and asymmetric pressure shadows have been used to deduce the sense of shear (Eisbacher 1970; Escher et al. 1975; Burg et al. 1981). The general sense of shear in the Kardamos part of the dome is top-to-the-S, ranging from top-to-the-SSW in the core, to top-to-the-SE in the lower part of the intermediate unit (Figs. 4, 5, 6). The ductile sense of shear at the higher part of the intermediate unit ranges from top-to-SE to top-to-SW.

The shear zone at the contact between the intermediate and the lower unit is several tens of meters thick. Deformation in the intermediate unit is heterogeneous. Ductile deformation gradients are identified from the reduction in grain size and in porphyroclast content in orthogneisses. More specifically, strongly foliated meta-igneous and meta-sedimentary rocks are separated by mylonitic to ultramylonitic shear zones (Fig. 7a, b) inclined <45° to the main foliation, which is bent into the shear planes. This shear zone has, in many places, been reactivated as brittle fault.

The Eastern Kardamos Detachment (EKD, Figs. 1, 6, 7c, d) is a normal fault that delineates the SE boundary of the Kesebir–Kardamos dome (Krohe and Mposkos 2002). It cuts through orthogneisses of the intermediate unit and separates the meta-ophiolite unit (Kimi unit) in the east from the Kardamos complex in the west. In the mapped area, the fault plane is sub–parallel to the main foliation
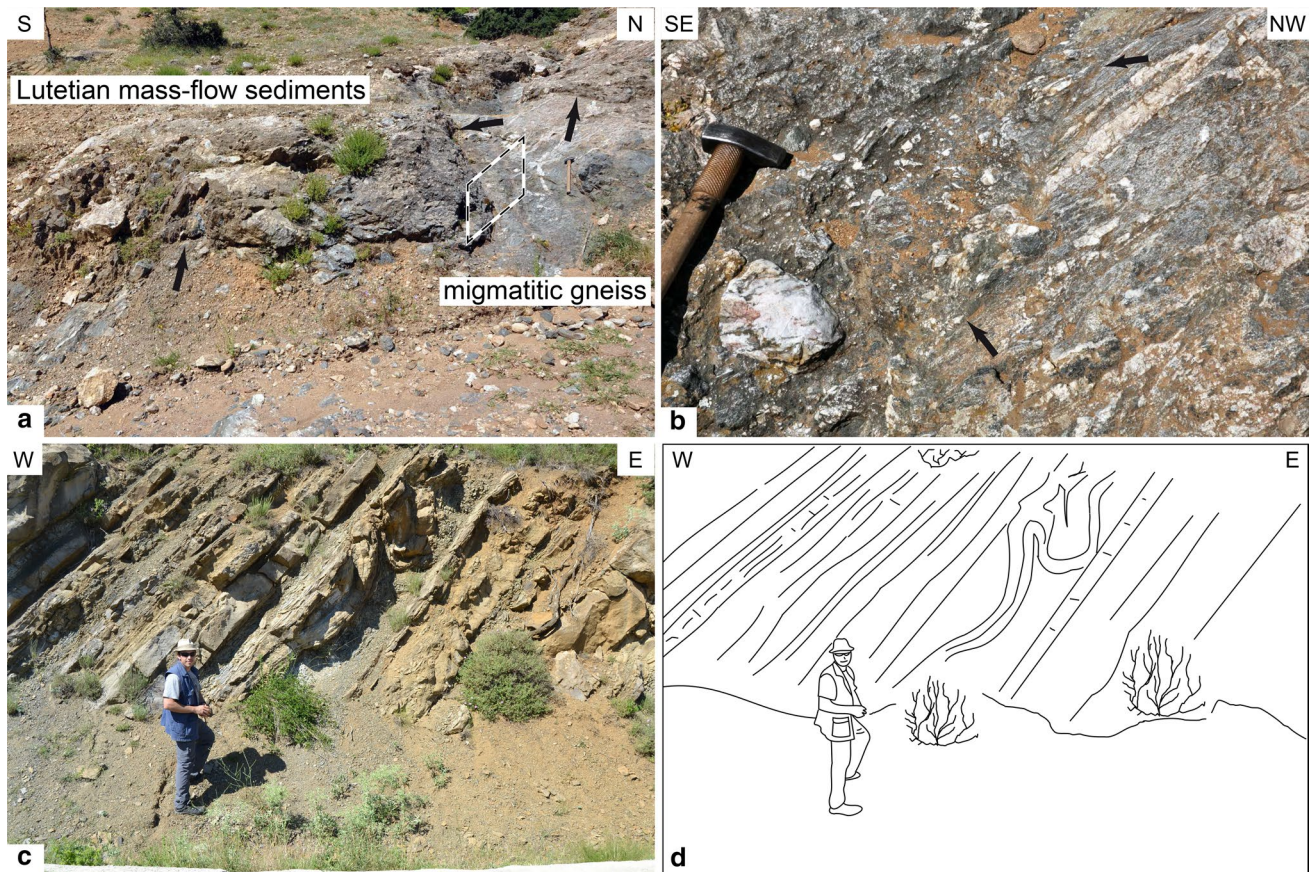
Fig. 3 a Sediments from the upper unit (Lutetian–Priabonian) unconformably resting on migmatitic amphibolites of the intermediate unit (location: N41°11′52.8″; E25°31′3.036″). Rhomb-shaped box contains the unconformity shown in detail in **b. c** Slump (sketched in **d**) in sediments of the *upper* unit (location: N41°12′50.11″; E25°34′38.892″)

and is defined by phyllonitic layers dipping towards the SE (at ca 40°) with S–C' fabrics (Fig. 7d) and sheared quartz veins indicating normal sense of movement. Such observations suggest that the fault overprints a ductile detachment. Mylonitic orthogneisses that have experienced grain-size reduction occur next to the phyllonites. These fabrics come in line with the observations of Bonev et al. (2006) further north in Bulgaria who suggested a deformation continuum from ductile to brittle conditions.

Porphyroclast rotation and non-coaxial flow

Locally, feldspar porphyroclasts in core augen-gneisses show opposite senses of rotation with respect to the regional top-to-the-S shearing. Several workers (e.g. Ghosh and Ramberg 1976; Passchier 1987; Wallis et al. 1993; Xypolias 2010) have argued that the rotation of rigid porphyroclasts in viscously deforming rocks may correspond to a coaxial component of the flow. The flow components are quantified by the kinematic vorticity number (Wk), which is a measure of relative coaxial/non coaxial flow

(Wk = 0 for pure shear and Wk = 1 for simple shear). The relationship between the kinematic vorticity number and the degree of non-coaxial deformation is not linear (c.f. Law et al. 2004; Forte and Bailey 2007). Studies on vorticity utilized the theoretical study of Jeffery (1922), who described the motion of elliptical rigid particles in a viscous fluid. To investigate the co-axial contribution to the flow, we employed the R–φ method (Fig. 8) as modified by Wallis et al. (1993). The aspect ratio (R) and the orientation of the inclusion relative to the shear plane (φ) are reported in a two-dimensional plot. A cut-off value (Rc) is chosen for R where the inclusions seem to have a stable orientation (i.e. $\varphi < 45°$). The mean kinematic vorticity number Wm can be calculated when Rc is known (Passchier 1987; Wallis et al. 1993) using the formula:

$$Wm = \frac{Rc^2 - 1}{Rc^2 + 1} \tag{1}$$

The mean vorticity number is not an instantaneous property; it is integrated over time and space and its validity relies on several assumptions, in particular that the flow is stable

Fig. 4 Structural measurements from the western part of the mapped area. Equal-area net, lower-hemisphere projection
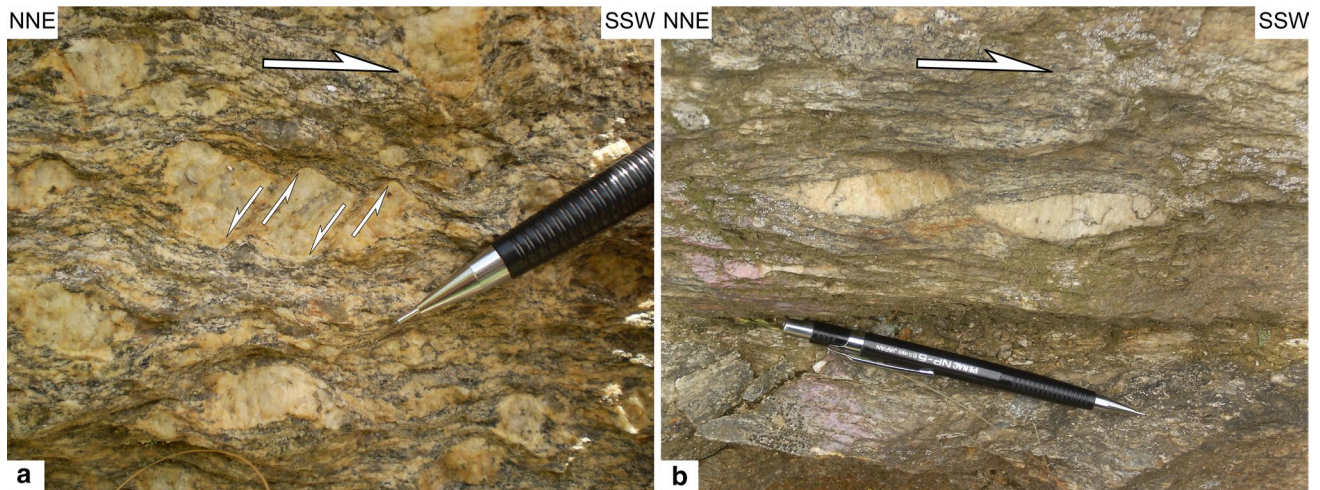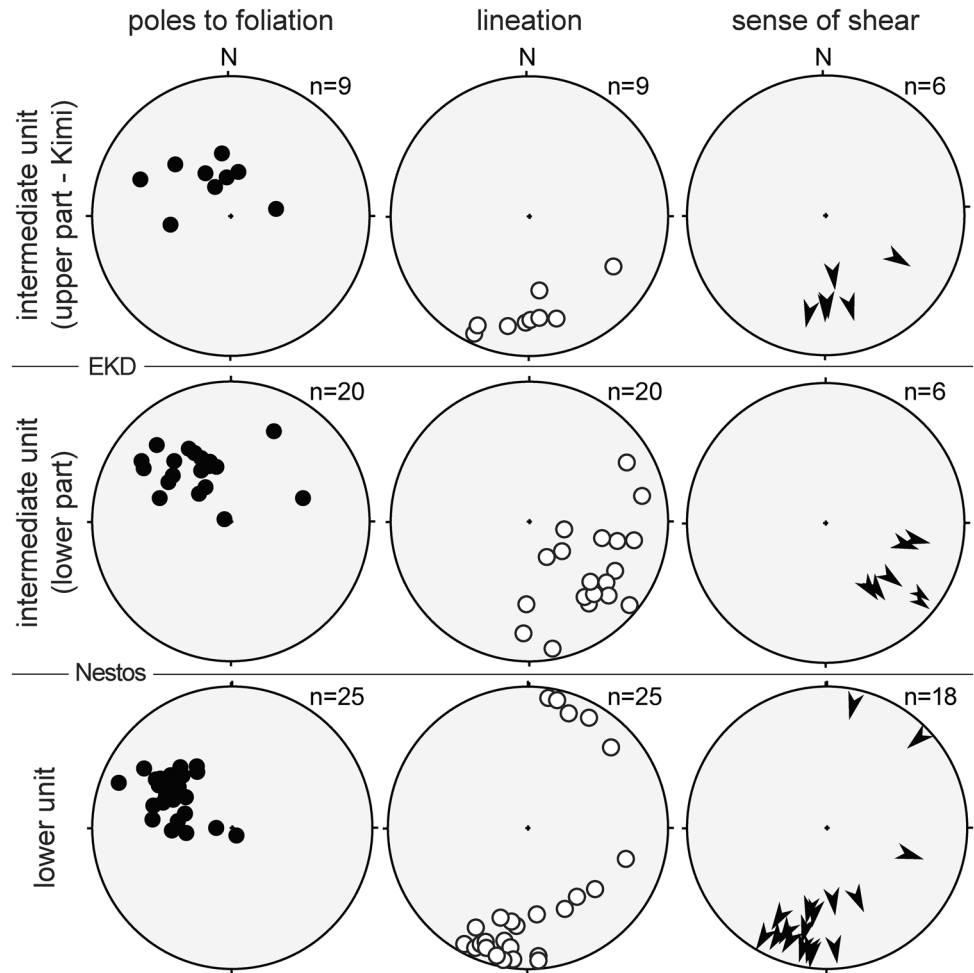

Fig. 5 Ductile deformation and kinematic indicators from the *lower* unit. **a** Domino-type fragmented feldspar porphyroclast in augen gneiss with top-to-the-SSW sense of shear (location: N41°16′04.2″; E25°28′10.2″). **b** Sigma-shaped clasts of alkali feldspar from augen gneisses indicating top-to-the-SSW sense of shear (location: N41°15′47.9″; E25°28′22.2″)
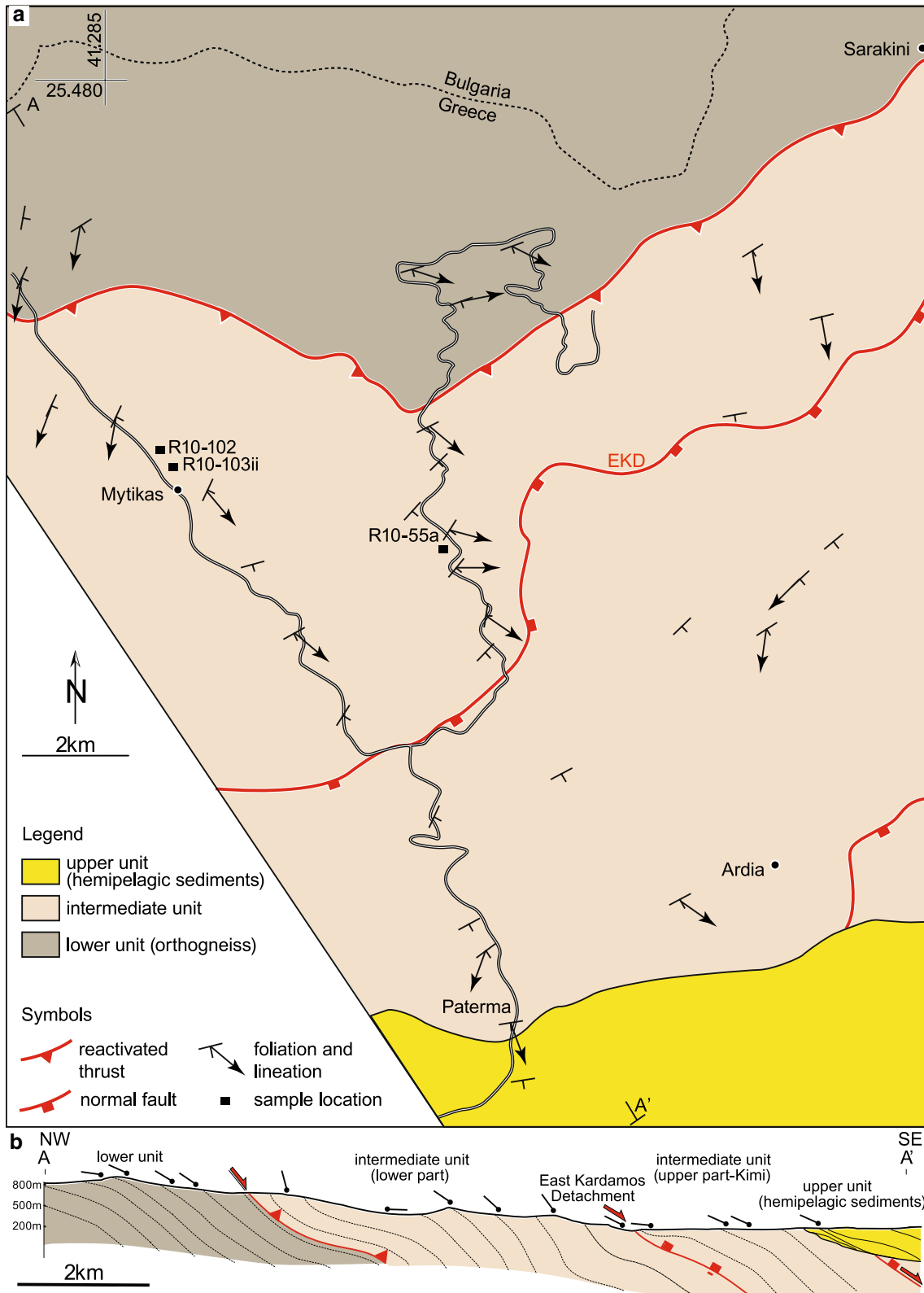
Fig. 6 **a** Structural and geological map of the southern part of the Kesebir–Kardamos dome in Greece with sample locations. **b** Cross-section A–A' indicated in a. *dotted lines* trace of foliation
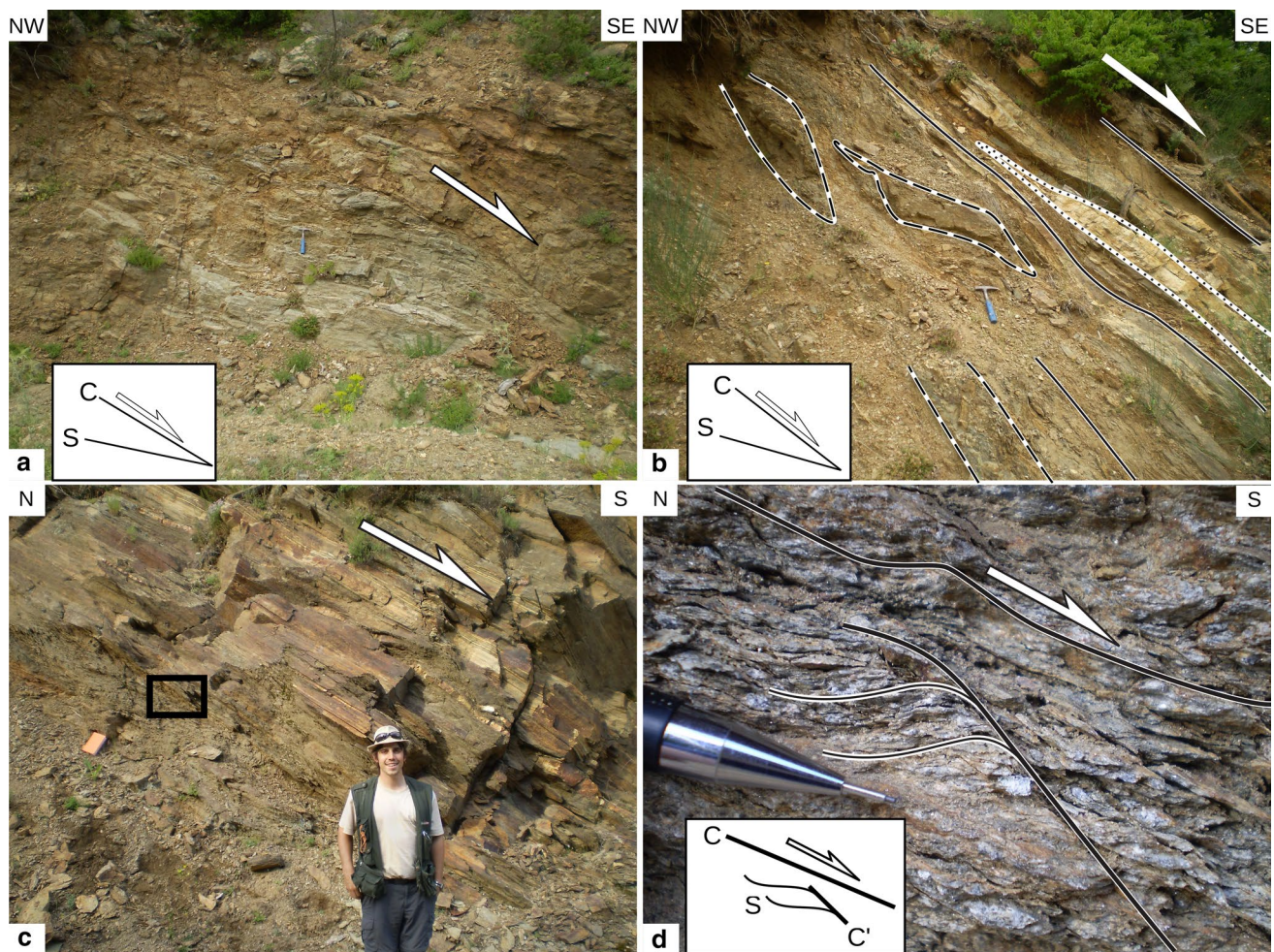
Fig. 7 a Mylonitic quartzo-feldspathic gneiss of the intermediate unit (location: N41°14′54.2″; E25°29′20.4″). The S–C fabric indicates a top-to-the-SE sense of shear. **b** Ductile mylonitic shear zone separating the lower from the intermediate unit. The shear zone exhibits a top-to-the-SE sense of shear (location: N41°15′09.4″; E25°28′58.5″) with a marble layer (*dotted line*) and amphibolite boudins (*dashed line*). **c** The Eastern Kesebir Detachment Zone in the southern part of the Kesebir–Kardamos dome. (location: N41°14′06.8″; E25°40′46.1″). **d** detail of the phyllonitic zone (*box* in **c**)

and in plane strain, and that the clasts are bonded to the viscous matrix and do not interact. The method also assumes that all rigid clasts rotate in the same sense, in accordance with the sense of shear, until they reach a stable position at a low angle to the shear plane. For any flow regime that includes a pure shear component, not all particles are free to rotate continuously; particles with an aspect ratio above a critical value will reach a stable position (Wallis et al. 1993).

These mean kinematic vorticity values amount to ca 40% of the total coaxial deformation observed (Fig. 8f). The five studied outcrops are within 50 m from each other but the measurements were made on outcrop sections (ca 2×2 m) which were parallel to the lineation and perpendicular to the foliation as required by the plane-strain requirement (location: N41°15′47.9″; E25°28′22.2″).

Petrology and metamorphic conditions

Analytical methods

Major-element mineral analyses and elemental maps were conducted at ETH–Zurich, Switzerland. We used a Jeol JXA 8200 electron probe micro-analyzer equipped with 5 wavelength dispersive spectrometers operating at an accelerating voltage of 15 kV. The electron-beam diameter was 2 μm and the beam current was 20 nA. Natural and synthetic materials were used as standards and a CITZAF correction procedure was applied. The counting time for each analysis was 60 s per element.
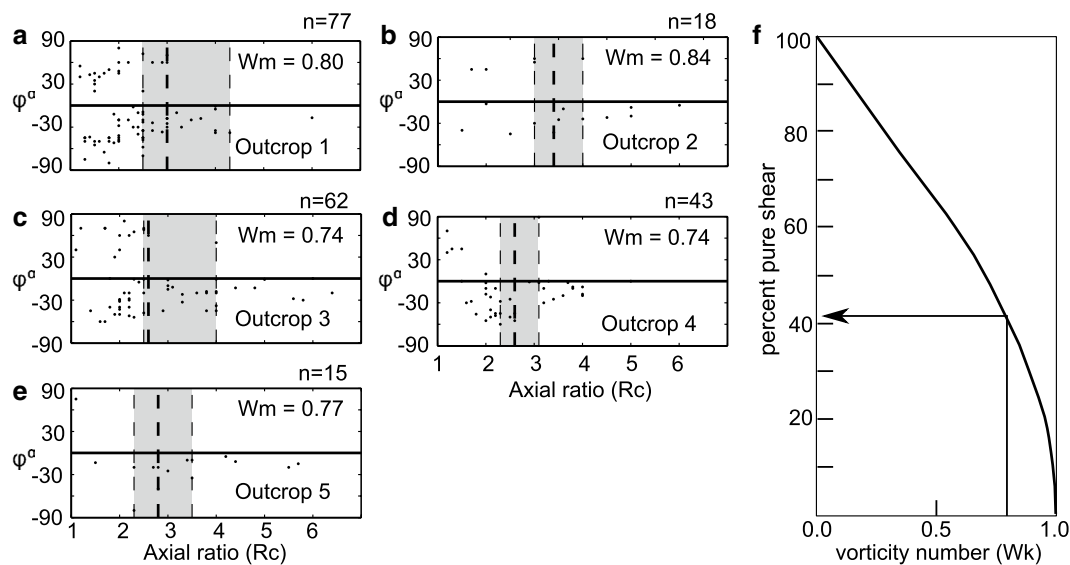
Fig. 8 **a–e** *Plots* of aspect ratio against inclination with respect to the main foliation for feldspar porphyroclasts. All measurements were taken on the kinematic plane defined by the lineation and the vertical to the foliation. *Dashed lines* are cut-off values (Rc) of objects with stable position (inclination <45°). The *shaded* field covers the uncertainty; *n* denotes the number of measurements in each outcrop. Wm indicates the mean vorticity number. The average Wm of the five outcrops studied is 0.78. **f** Relationship between the kinematic vorticity number (Wk) and the component of pure shear (after Law et al. 2004). The mean vorticity number Wm = 0.78 (averaged over the 5 outcrops—**a–e**) translates into ca 40% pure-shear component

Table 1 Mineralogy of studied samples from the intermediate unit. The mineral order does not infer relative abundance

Sample name	R10-102	R10-103M	R10-55a
Rocktype		Metapelitic schist	
Mineral			
Quartz	+	+	+
Plagioclase	+	+	+
Kyanite	+	+	+
Garnet	+	+	+
Biotite	+	+	+
Staurolite			+
Muscovite	+	+	
Paragonite			+
Chlorite	+	Traces	Traces
K-Feldspar	Traces		Traces
Allanite	+		
Rutile	+	+	+
Ilmenite		+	+

Petrographic observations and mineral chemistry

Two samples from the intermediate unit were used for detailed petrographic investigation because they exhibit minor retrogression. Their mineral assemblages are summarized in Table 1. Representative mineral analyses are given in Tables 2 and 3.

Sample R10-103ii is a quartz-mica-garnet schist (Fig. 9a–d). The rock contains, in decreasing abundance, quartz, white mica (muscovite-rich), garnet, kyanite, biotite, plagioclase, rutile ± ilmenite. White mica (Si: 3.15–3.25 atoms per formula unit—apfu) is well crystallized and exhibits asymmetric shapes (e.g. Eisbacher 1970). Garnet is porphyroblastic, ranging from 0.5 to 1.5 mm in diameter. It is relatively homogeneous with an average composition (in molar fractions) of $Prp_{0.23}Grs_{0.10-0.11}Alm_{0.66-0.68}Sps_{0.00-0.02}$; Mg#: 0.24–0.25 [where Mg# is the molar ratio Mg/(Mg + Fe)]. Kyanite varies in size from very fine grains to deformed grains reaching 1 mm in length (Fig. 9b). Biotite (Mg#: 0.49–0.50) selvedges replace garnet rims and develop along cracks within garnet porphyroblasts (Fig. 9c) and along foliation surfaces (Fig. 9a). Sodic plagioclase ($An_{0.20}$) occurs in small amounts in the matrix. Rutile, partly replaced by ilmenite, occurs as inclusions in garnet.

Sample R10-55a is a coarse-grained, quartz-mica-garnet schist. The rock is composed of inter-layered mica-rich and quartz-rich layers of millimeter scale. It contains a significant (>20 vol.%) amount of garnet porphyroblasts that can reach up to 2 cm in diameter. Quartz inclusions form trails in garnet (Fig. 10). The main paragenesis is, in order of decreasing mineral abundance, quartz, white mica (paragonite-rich), garnet, plagioclase, biotite, kyanite, staurolite ± rutile ± ilmenite (Fig. 9e, f). Garnet porphyroblasts are chemically zoned with

Table 2 Representative electron microprobe mineral analyses of sample R10-103ii

Mineral	Bio	Bio	Bio	Ms	Ms	Ms	Ms	Ms	Ms	Grt	Pl
Sample #	s11	s23	s10	s31	1t1	14t1	2lin1	7lin1	8lin1	20lin2	30lin1
SiO_2	34.81	36.37	35.22	47.21	48.79	47.45	49.03	48.60	49.19	38.05	63.38
TiO_2	1.88	0.33	1.35	0.73	0.48	0.59	0.49	0.48	0.40	0.11	0.00
Al_2O_3	18.11	19.37	19.59	32.88	31.11	32.37	29.88	30.84	30.26	21.48	22.73
Fe_2O_3				0.00	0.00	0.00	0.00	0.00	0.00		0.08
FeO^t	18.62	18.49	18.99	2.93	2.61	3.14	3.13	2.71	2.77	30.83	
MnO	0.10	0.00	0.11	0.00	0.01	0.01	0.00	0.00	0.00	0.59	0.03
MgO	10.29	9.99	10.51	1.04	2.08	1.17	2.48	2.19	2.38	6.03	0.00
CaO	0.31	0.20	0.01	0.00	0.00	0.01	0.00	0.00	0.00	3.65	4.23
Na_2O	0.18	0.13	0.18	0.71	1.03	0.54	0.67	0.67	0.55	0.01	9.00
K_2O	7.12	7.11	8.29	9.38	8.81	9.66	9.24	9.47	9.36	0.00	0.15
Cr_2O_3	0.12	0.04	0.07	0.12	0.09	0.05	0.08	0.04	0.08	0.10	0.00
Sum	91.54	92.02	94.33	95.00	95.00	95.00	95.00	95.00	95.00	100.86	99.61
Si	2.722	2.803	2.685	3.158	3.246	3.180	3.277	3.246	3.280	2.974	2.810
Ti	0.111	0.019	0.077	0.037	0.024	0.030	0.025	0.024	0.020	0.006	0.000
Al	1.669	1.759	1.760	2.592	2.440	2.557	2.354	2.428	2.379	1.978	1.188
Fe^{3+}										0.000	0.003
Fe^{2+}	1.218	1.192	1.211	0.164	0.145	0.176	0.175	0.151	0.154	2.015	0.000
Mn	0.006									0.039	0.001
Mg	1.200	1.148	1.194	0.104	0.207	0.116	0.247	0.218	0.236	0.702	0.000
Ca	0.026	0.016	0.001	0.000	0.000	0.001	0.000	0.000	0.000	0.306	0.201
Na	0.027	0.019	0.027	0.091	0.132	0.070	0.087	0.087	0.071	0.002	0.773
K	0.710	0.699	0.806	0.800	0.748	0.826	0.788	0.807	0.797	0.000	0.008
Cr	0.008	0.002	0.004	0.006	0.005	0.003	0.004	0.002	0.004	0.006	0.000
Sum	7.697	7.657	7.772	6.952	6.948	6.959	6.956	6.962	6.942	8.029	4.985

spessartine-rich cores and a rimward increase in Mg# (Fig. 10); their composition can be described by the formula: $Prp_{0.07-0.21}Grs_{0.23-0.15}Alm_{0.63-0.59}Sps_{0.07-0.04}$; Mg#: 0.10–0.26. Kyanite and sodic plagioclase (An_{18-25}) occur next to paragonite (Si: 3.04–3.17apfu); staurolite (Mg#: 0.25–0.26) and biotite (Mg#: 0.63–0.66) are also found in the domains where kyanite and plagioclase are present (Fig. 11).

P–T estimates

Following a detailed study under the petrographic microscope and reconnaissance EMP analyses, sample R10-103ii was selected as the most appropriate for robust *P–T* estimates. An important criterion in choosing this sample was the observation that garnet porphyroblasts are compositionally homogeneous and show minor retrogression. An equilibrium phase-diagram section was used to estimate the metamorphic conditions of sample R10-103ii. The phase-diagram section was calculated using the Perplex software package (http://www.perplex.ethz.ch/) that predicts the stable minerals for a given chemical composition by minimizing the Gibbs free energy (Connolly 2005) using the thermodynamic database of Holland and Powell 1998 (updated 2002).

The solid solution models used in the calculations are given in Table 4. The input bulk-rock composition for the phase equilibrium calculations was obtained from modal analysis of the mineral assemblage present in thin section (c.f. Tajčmanová et al. 2006; Nagel et al. 2011). A total of 400 mineral microprobe measurements was used to estimate the bulk-rock composition. The input amount of water in the bulk-rock composition was estimated in such a way that the mineral assemblage is water saturated in sub-solidus conditions and no free water coexists with melt after the solidus curve is crossed. This estimate is consistent with studies that infer that the amount of water in high-grade metamorphic rocks is less than 0.03 wt.% (Clemens and Vielzeuf 1987). The *P–T* conditions for sample R10-103ii were estimated using compositional isopleths of plagioclase and garnet in an isochemical phase-diagram section (Fig. 12). The estimated *P–T* conditions are 1.2 ± 0.1 GPa and 730 ± 40 °C. These conditions are within a phase field that includes melt, but its modal proportion is <5 vol.%.

Table 3 Representative electron microprobe mineral analyses of sample R10-55a

Mineral	Ms (Pg)	Ms (Pg)	St	Bt	Bt	Grt	Grt	Pl
Sample #	ena_3	ena92	ena96	ena97	ena90	27-55aii	80-55aii	pl1
SiO_2	48.91	48.64	26.20	36.77	36.79	37.90	38.44	61.48
TiO_2	0.16	0.16	0.25	1.23	1.32	0.17	0.07	0.00
Al_2O_3	39.22	39.59	56.37	19.91	18.64	20.97	21.68	22.81
Fe_2O_3								0.11
FEO'	0.48	0.63	11.50	13.49	14.95	28.71	27.68	0.10
MnO	0.00	0.00	0.38	0.07	0.10	3.24	2.13	0.01
MgO	0.10	0.22	2.29	14.68	14.01	1.75	5.56	0.00
CaO	0.29	0.39	0.01	0.03	0.25	8.28	5.59	6.03
Na_2O	4.45	4.24	0.00	0.58	0.54	0.06	0.00	
K_2O	0.94	1.68	0.01	8.31	7.65	0.00	0.00	0.05
Cr_2O_3	0.03	0.06	0.04	0.08	0.01	0.03	0.00	0.01
Sum	94.58	95.60	97.06	95.15	94.25	101.10	101.15	98.26
Si	3.106	3.074	3.791	2.700	2.741	3.003	2.985	2.772
Ti	0.008	0.008	0.027	0.068	0.074	0.010	0.004	
Al	2.936	2.949	9.613	1.723	1.636	1.958	1.984	1.212
Fe^{3+}						0.000	0.000	0.004
Fe^{2+}	0.025	0.033	1.392	0.828	0.931	1.902	1.797	0.004
Mn			0.047	0.005	0.006	0.217	0.140	
Mg	0.010	0.020	0.494	1.607	1.556	0.207	0.644	
Ca	0.020	0.027	0.002	0.002	0.020	0.703	0.465	0.291
Na	0.548	0.520	0.000	0.082	0.077	0.009	0.001	0.671
K	0.076	0.135	0.003	0.778	0.727			0.003
Cr	0.002	0.003	0.005	0.005	0.000	0.002		
Sum	6.729	6.769	15.374	7.798	7.769	8.011	8.020	4.957
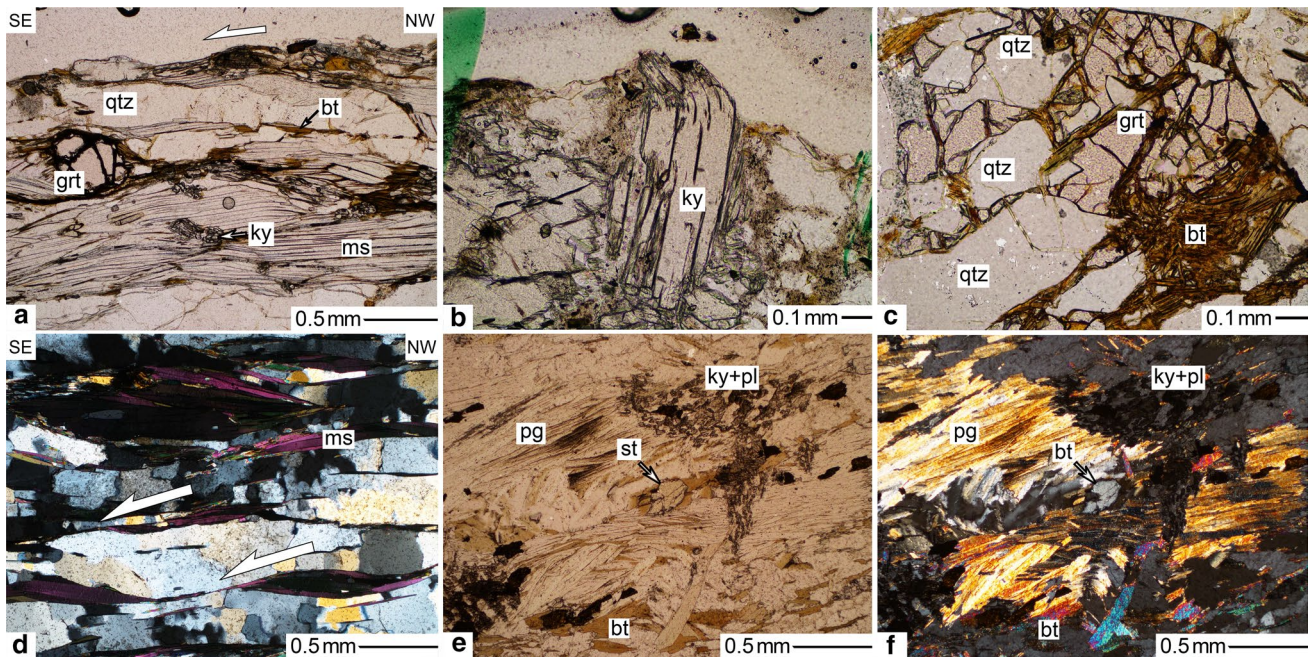
Fig. 9 Photomicrographs displaying the most important textures used in the petrographic analysis. Mineral abbreviations after Siivola and Schmid (2007). **a–d** sample R10-103ii, **e–f** sample R10-55a. Photomicrographs d and f are taken with crossed polars
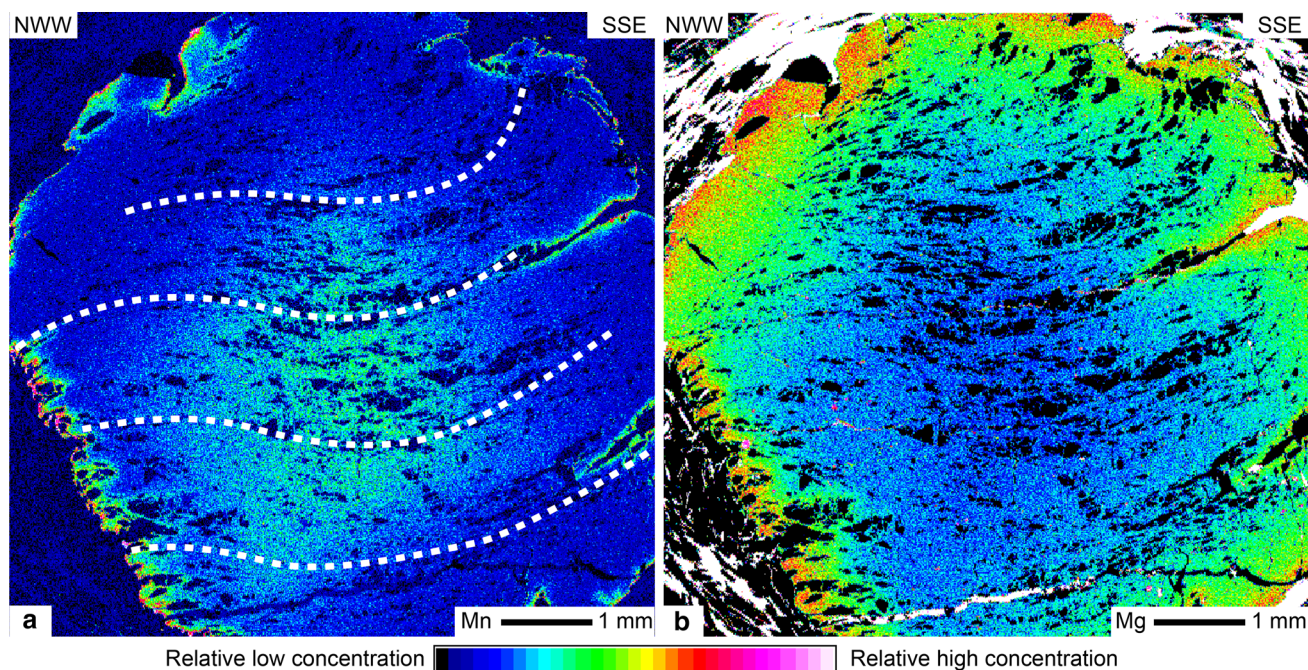
Fig. 10 Manganese (**a**) and magnesium (**b**) maps of a garnet porphyroblast from sample R10-55a. The *thin dashed lines* indicate quartz-inclusion trails
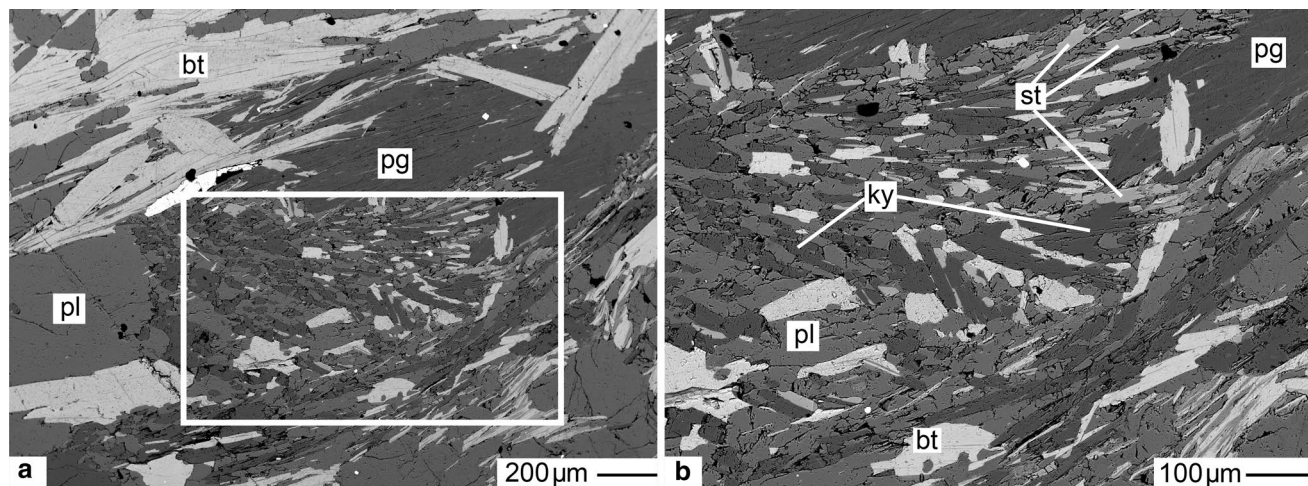

Fig. 11 Backscattered-electron (BSE) image from sample R10-55a. **a** Small laths of kyanite and plagioclase have crystallized next to paragonite. **b** Detail of **a** showing fine-grained staurolite and biotite

Geochronology

Sample preparation: analytical methods

Zircons were separated at ETH–Zurich. Over 1 kg of metapelite sample R10-102 was crushed using shockwaves in SELFRAG (http://www.selfrag.com). Zircons were then extracted using a Franz isodynamic magnetic separator, heavy liquids (methylene iodide) and finally hand-picking

under a binocular microscope. Selected zircon grains were mounted together with zircon standard grains 91,500 and TEMORA–1 in epoxy resin. They were then sectioned and polished to approximately half their original thickness, gold coated, and investigated using cathodoluminescence (CL) imaging. In-situ U–Pb isotope analyses were made with SHRIMP–II at the Center of Isotopic Research (CIR) at VSEGEI, St. Petersburg, Russian Federation. Measuring conditions are given in Moulas et al. (2013).

Table 4 Solid solutions used in the equilibrium phase-diagram calculations. More details at http://www.perplex.ethz.ch/

Mineral/phase	Solution model	References
Biotite	Bio (TCC)	Tajčmanová et al. (2009)
Feldspars	Feldspar	Newton et al. (1980); Fuhrman and Lindsley (1988)
Garnet	Gt (GCT)	Ganguly et al. (1996)
Ilmenite	IlGkPy	Ideal
White mica	Mica (CHA1)	Coggon and Holland (2002); Auzanneau et al. (2010)
Chlorite	Chl (HP)	Holland et al. (1998)
Staurolite	St (HP)	parameters from Thermocalc
Chloritoid	Ctd (HP)	White et al. (2000)
Cordierite	hCrd	Ideal
Melt	melt (HP)	Holland and Powell (2001); White et al. (2001)
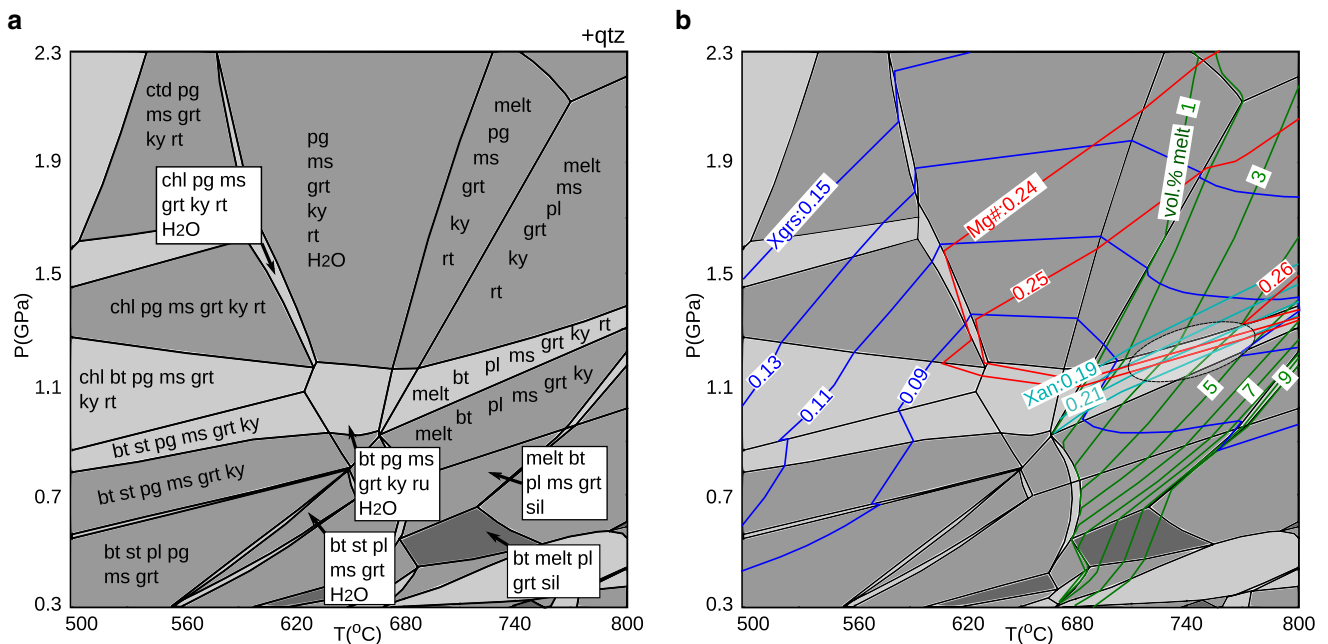
Fig. 12 a Phase-diagram section for sample R10-103ii. **b** Mineral assemblage and compositional isopleths of plagioclase (X_{An}) and garnet (X_{Grs} and Mg#) are used to estimate the *P–T* conditions recorded by this sample (indicated by an *ellipse*)

Zircon description and ages

Zircons from quartz-mica-garnet-schist R10-102 are elliptic with rounded edges, measuring 100–200 μm along their length. Cathodoluminescence images (Fig. 13) revealed cores surrounded by inclusion-rich rims. The preservation of oscillatory zoning in some of the detrital cores indicates their magmatic origin (Corfu et al. 2003). Based on the CL patterns, three textural zircon domains are distinguished: An inner detrital core, an inclusion-rich inner rim and, in some cases, a thin bright outer rim (Fig. 13). The cores have high Th/U ratios (>0.1, see supplementary material) indicating magmatic crystallization; by contrast, the rims show low Th/U ratios (<0.1) that are typical of metamorphic zircons (Teipel et al. 2004). Cathodoluminescence
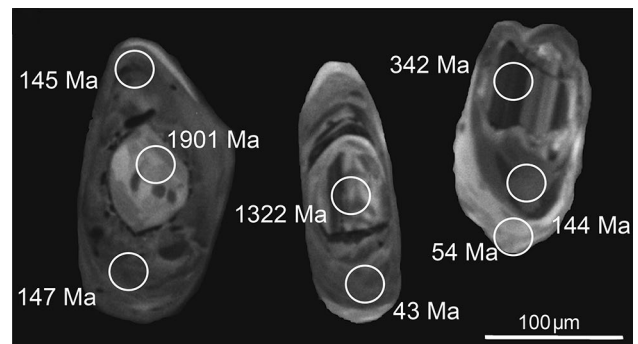

Fig. 13 CL images with spot analyses of representative zircons from sample R10-102. Thin bright rims in some of the zircons indicate Pb loss

images of all measured zircons and associated tables are given in the supplementary material. The concordant ages of the cores range between 1.9 and 0.3 Ga (Fig. 14a–b). Most of the zircon rims yielded a lower-intercept age of 144.8 ± 1.1 Ma in the Tera–Wasserburg diagram (Fig. 14c). Four rims yielded two ages, one at 53.6 ± 1.1, the other at 44.3 ± 1.3 Ma (Fig. 14d).

Synthesis and discussion

Our new structural and kinematic data testify to a bulk top-to-the-S (from SSW to SE) sense of shear in the lower and intermediate units of the Eastern Kardamos Dome. This sense of shear is consistent with the one previously reported by Bonev et al. (2006) further north in Bulgaria. The vorticity estimates from five outcrops (Fig. 8) are similar to those obtained by Bonev et al. (2006) on two samples (Wm: 0.7–0.8). Consistency of vorticity numbers is no final proof for the relatively large amount of coaxial deformation. The fact that flow is not

in plane strain and that clast rotation is a three-dimensional problem have been used by Li and Jiang (2011) to dispute the method. In addition, the fact that ductile flow is generally not steady introduces further uncertainty factors. Furthermore, imperfect bonding between clasts and the matrix may lead to back rotation for some initial orientations (Ceriani et al. 2003). Therefore, the vorticity results should be viewed with caution in terms of deformation regime and relative importance of coaxial versus non-coaxial strain.

Rotated garnets that grew syn-kinematically show a top-to-the-SE sense of shear (Fig. 10). The chemical zoning of these garnets indicates prograde (increasing temperature) growth (e.g. Hollister 1966; Tracy 1982; Harris et al. 2004). Bended kyanite crystals (Fig. 9b) indicate pre-to syn-kinematic growth. White mica within shear bands is also consistent with syn-metamorphic top-to-the-SE sense of shear (Fig. 9). These results are consistent with the regional sense of shear determined for the intermediate unit on the western flank of the Kesebir dome in Bulgaria (Bonev 2006; Bonev et al. 2006).
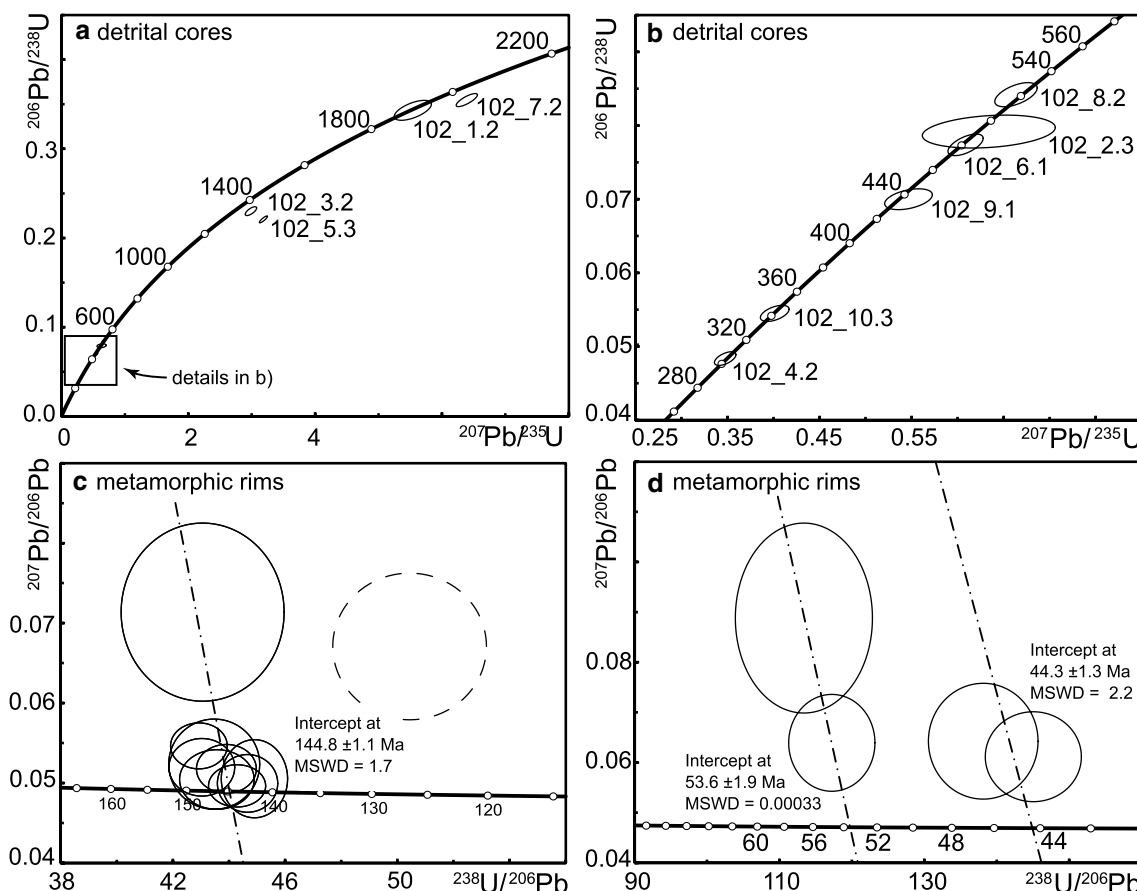

Fig. 14 Concordia and Tera–Wasserburg diagrams for zircons from sample R10-102 analyzed by SHRIMP-II. **a–b** Concordia diagrams for the detrital cores. **c–d** Tera–Wasserburg diagrams for the meta-morphic rims. The measurement shown in *dashes* (**c**) was not used in the age determination

Our phase-diagram section (Fig. 12) calculations indicate that the near-peak *P–T* mineral assemblage recorded in the metapelites involved the coexistence of garnet, white mica, kyanite and biotite (Fig. 12a). The pre- to syn-kinematic character of kyanite, white mica and especially garnet suggests that these minerals experienced top-to-the-SE ductile deformation at ca. 1.2 GPa and 730 °C, i.e. near the transition between amphibolite and eclogite facies (Spear 1993; Bucher and Frey 2002). Mposkos and Liati (1993) obtained comparable upper amphibolite-facies conditions (ca 1.4 GPa and 680 °C) and showed that this was followed by a retrograde event at 1.0 GPa and 650 °C. Krohe and Mposkos (2002) proposed that the East Kardamos Detachment, which is characterized by top-to-the-S kinematics, is responsible for the exhumation of the high-grade rocks. The top-to-the-SE shearing can be interpreted either as ductile thrusting (i.e. a folded thrust) or ductile normal faulting. Similar ductile fabrics developed under similar metamorphic conditions in similar lithologies have been attributed to thrusting in the western parts of the dome (Burg et al. 1996; Bonev 2006; Bonev et al. 2006). Map continuity of such fabrics that exist in both hanging wall and footwall of the East Kardamos Detachment is an argument to ascribe SE-ward shearing to the regional thrusting that preceded the more localized, lower grade ductile normal faulting. In addition, the zoning of the syn-kinematic garnets additionally suggests that this shearing event occurred during heating, which can be viewed as syn-thrusting/thickening (*not extensional thinning*) prograde metamorphism, even if the recrystallization of paragonite, biotite and syn-kinematic white mica suggests that the top-to-the-SE shearing continued upon cooling.

Zircon geochronology (Fig. 14) and U/Th ratios of zircon rims allowed us to distinguish three discrete ages related to metamorphism: 145, 53 and 44 Ma (see supplementary material). We interpret the 145 Ma zircon age as the time most likely corresponding to closure of the U-Pb isotopic system in this mineral after the 730 °C peak temperature (see also Reischmann and Kostopoulos 2002). This is consistent with the results of Krenn et al. (2010) who suggested that the age of the major amphibolite-facies (700–750 °C; 1.0–1.2 GPa) ductile shearing in the intermediate imbricate units of central Rhodope occurred at ~145 Ma (Fig. 15). The younger ages at 53 and 44 Ma are contemporaneous with the well-established Eocene magmatic activity in the region (Fig. 15). These younger ages fall within the range of ^{40}Ar-^{39}Ar mineral ages (64–34 Ma) from the intermediate unit (Bonev et al. 2013). Such cooling ages come in line with lower-temperature (ca 300–350 °C) K-Ar mica ages of 39 and 42 Ma reported for the southern parts of the KKD (Krohe and Mposkos 2002). Furthermore, the presence of Maastrichtian–Paleocene sediments atop the metamorphic pile of the intermediate

migmatitic unit (Goranov and Atanasov 1992; Bonev et al. 2006) imply that, at least in the northern part of the KKD, the intermediate unit was exhumed already by the Upper Cretaceous. This shows that the main syn-metamorphic thrusting had already ended by that time. In the southern parts of the KKD dome, the age of the oldest unconformable sediments is Lutetian (48–41 Ma; Caracciolo et al. 2012). Finally, low-temperature thermochronology data over the western Rhodope suggest cooling below 240 °C at 72 Ma (Kydonakis et al. 2014; Kounov et al. 2015; Schenker et al. 2015). Similar correlations between metamorphic ages and crystallization ages of plutons can also be observed in central Rhodope (Fig. 15).

Interestingly, the ages of granitoid pluton crystallization in the Rhodope become systematically younger from north to south as do the metamorphic ages of (U)HP rocks (Fig. 15). If this younging trend of isotopic ages is considered, then the Late Cretaceous and younger metamorphic ages obtained (e.g., ca 70–92 Ma for the Chepelare shear zone; Collings et al. 2016) cannot be explained by metamorphism in a subduction channel at great depths as their authors have contended. We propose that the post-Jurassic metamorphic ages recorded in the Rhodope represent crustal rather than deep subduction geodynamic processes. These ages may reflect metamorphic recrystallization due to local heat production or isotopic reset due to magmatism.

Conclusions

The Kesebir-Kardamos dome in northern Greece and southern Bulgaria exposes a nappe duplex formed during top-to-the-SE ductile shearing. The core of the dome is mostly made of orthogneisses and amphibolites (occasionally migmatitic). These core rocks are separated from marble, migmatitic amphibolites, mylonitic orthogneisses, paragneisses and calc-silicate gneisses of the intermediate thrust unit by a folded, mostly non-reactivated ductile thrust. The East Kardamos Detachment cuts, on a map-scale, the thrust and its hanging wall lithologies that reached peak *P–T* conditions of 1.2 GPa and 730 °C during ductile, top-to-the-SE shearing at or before 145 Ma. The syn-kinematic prograde growth of garnet up to peak conditions suggests thrusting of the intermediate unit on top of the lower unit of the RMC, as it has been advocated for the Nestos Suture Zone in Central Rhodope (e.g. Krenn et al. 2010). In eastern Rhodope, sediments unconformably covering migmatitic amphibolites of the intermediate unit demonstrate a deeply eroded orogenic crust as early as 65 Ma. On a regional scale, the new *P–T* and geochronological data presented here provide
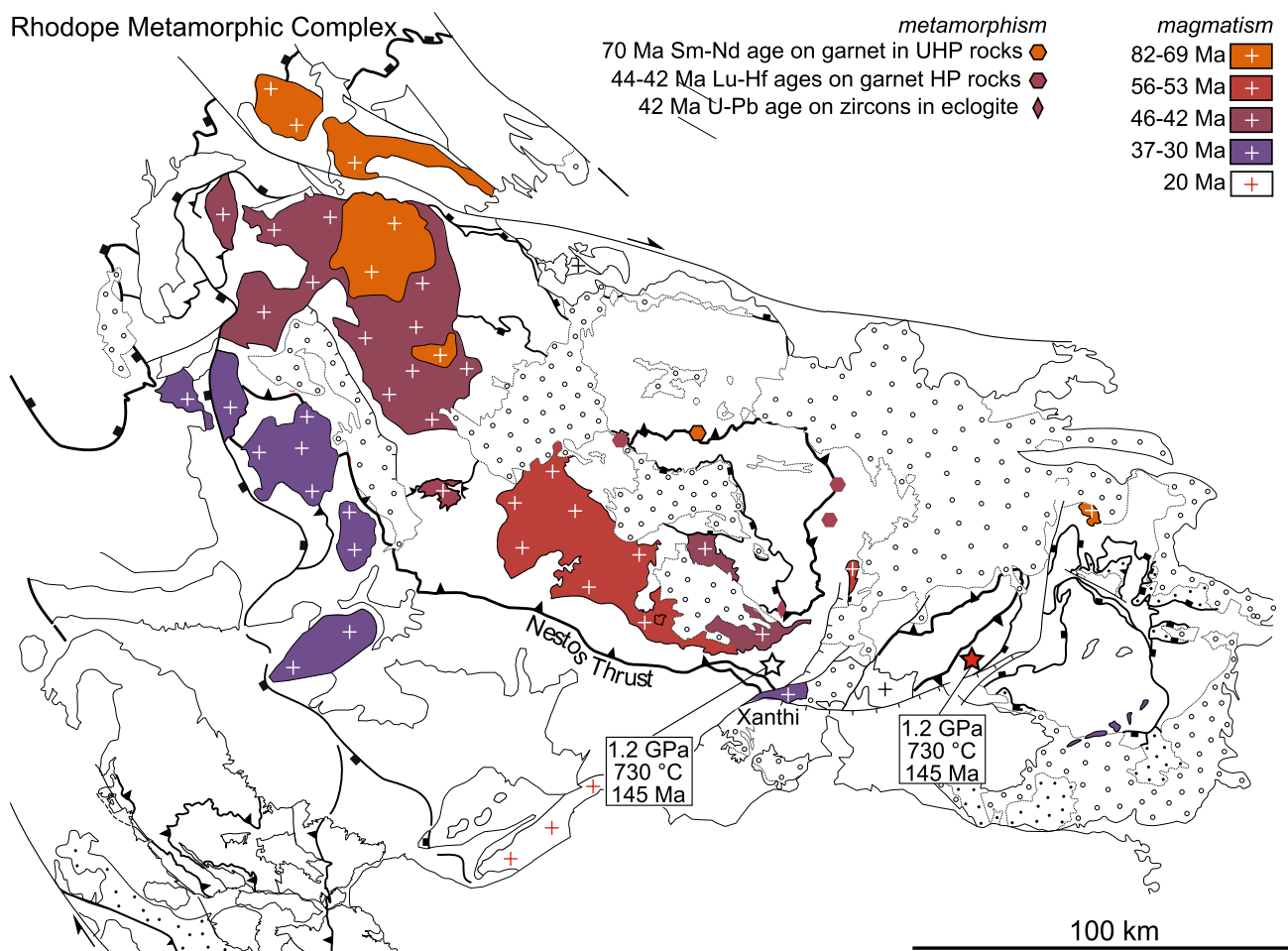
Fig. 15 Simplified map of the southern Rhodope displaying the zoning in granitoid ages (in Ma) (compilation after Burg 2012 and references therein; Zagorchev et al. 2012). Similarly aged *P–T–t* estimates for the intermediate unit from Krenn et al. (2010; indicated with a *white star*) and this study (indicated with a *red star*). Garnet Sm-Nd and Lu-Hf ages are after Collings et al. (2016) and Kirchenbaur et al. (2012). NSZ: Nestos Shear Zone

evidence that the intermediate unit of the Kesebir–Kardamos dome is the eastern continuation of the Late Jurassic–Early Cretaceous (ca 145 Ma) Nestos Suture Zone.

References

Auzanneau E, Schmidt MW, Vielzeuf D, Connolly JAD (2010) Titanium in phengite: a geobarometer for high temperature eclogites. Contrib Mineral Petrol 159:1–24. doi:10.1007/s00410-009-0412-7

Bauer C, Rubatto D, Krenn K, Proyer A, Hoinkes G (2007) A zircon study from the Rhodope metamorphic complex, N-Greece: Time record of a multistage evolution. Lithos 99:207–228. doi:10.1016/j.lithos.2007.05.003

Baziotis I, Mposkos E, Asimow PD (2008) Petrogenesis of Ultramafic Rocks from the Ultrahigh-pressure Metamorphic Kimi Complex in Eastern Rhodope (NE Greece). J Petrol 49:885–909. doi:10.1093/petrology/egn010

Berthé D, Choukroune P, Jegouzo P (1979) Orthogneiss, mylonite and non coaxial deformation of granites: the example of the South Armorican Shear Zone. J Struct Geol 1:31–42. doi:10.1016/0191-8141(79)90019-1

Bonev N (2006) Cenozoic tectonic evolution of the eastern Rhodope massif (Bulgaria): basement structure and kinematics of syn- to postcollisional extensional deformation. Geol Soc Am Sp Pap 409:211–235. doi:10.1130/2006.2409(12)

Bonev N, Beccaletto L (2007) From syn- to post-orogenic Tertiary extension in the north Aegean region: constraints on the kinematics in the eastern Rhodope–Thrace, Bulgaria–Greece and the Biga Peninsula, NW Turkey. Geological Society, London. Sp Publ 291:113–142. doi:10.1144/SP291.6

Bonev N, Burg J-P, Ivanov Z (2006) Mesozoic–Tertiary structural evolution of an extensional gneiss dome—the Kesebir–Kardamos dome, eastern Rhodope (Bulgaria–Greece). Int J Earth Sci (Geol Rundsch) 95:318–340. doi:10.1007/s00531-005-0025-y

Bonev N, Spikings R, Moritz R, Marchev P, Collings D (2013) 40Ar/39Ar age constraints on the timing of Tertiary crustal extension and its temporal relation to ore-forming and magmatic processes in the Eastern Rhodope Massif, Bulgaria. Lithos 180–181:264–278. doi:10.1016/j.lithos.2013.05.014

Bosse V, Boulvais P, Gautier P, Tiepolo M, Ruffet G, Devidal JL, Cherneva Z, Gerdjikov I, Paquette JL (2009) Fluid-induced disturbance of the monazite Th–Pb chronometer: In situ dating and element mapping in pegmatites from the Rhodope (Greece, Bulgaria). Chem Geol 261:286–302. doi:10.1016/j.chemgeo.2008.10.025

Boyanov I, Ruseva M, Dimitrova E (1982) First find of Upper Cretaceous foraminifers in East Rhodopes. Geol Balc 12:20

Brun JP (1983) L'origine des dômes gneissiques: Modèles et tests. Bulletin de la Société Géologique de France 25:219–228

Brun J-P, Sokoutis D (2007) Kinematics of the Southern Rhodope Core Complex (North Greece). Int J Earth Sci (Geol Rundsch) 96:1079–1099. doi:10.1007/s00531-007-0174-2

Bucher K, Frey M (2002) Petrogenesis of Metamorphic Rocks, 7th edn. Springer, Berlin

Burg JP (2012) Rhodope: From Mesozoic convergence to Cenozoic extension. Review of petro-structural data in the geochronological frame. J Virtual Explor 42:2–44. doi:10.3809/jvirtex.2011.00270

Burg JP, Iglesias M, Laurent P, Matte P, Ribeiro A (1981) Variscan intracontinental deformation: the Coimbra—Cordoba shear zone (SW Iberian Peninsula). Tectonophysics 78:161–177. doi:10.1016/0040-1951(81)90012-3

Burg J-P, Ivanov Z, Ricou L-E, Dimor D, Klain L (1990) Implications of shear-sense criteria for the tectonic evolution of the Central Rhodope massif, southern Bulgaria. Geology 18:451–454. doi:10.1130/0091-7613(1990)018<0451:IOSSCF>2.3.CO;2

Burg J-P, Ricou L-E, Ivanov Z, Godfriaux I, Dimov D, Klain L (1996) Syn-metamorphic nappe complex in the Rhodope Massif. Structure and kinematics. Terra Nova 8:6–15. doi:10.1111/j.1365-3121.1996.tb00720.x

Burg J-P, Kaus BJP, Podladchikov YY (2004) Dome structures in collision orogens: mechanical investigation of the gravity/compression interplay. Geol Soc Am Sp Pap 380:47–66. doi:10.1130/0-8137-2380-9.47

Caracciolo L, Critelli S, Innocenti F, Kolios N, Manetti P (2011) Unravelling provenance from Eocene-Oligocene sandstones of the Thrace Basin, North-east Greece. Sedimentology 58(7):1988–2011

Caracciolo L, von Eynatten H, Tolosana-Delgado R, Critelli S, Manetti P, Marchev P (2012) Petrological, geochemical, and statistical analysis of eocene–oligocene sandstones of the Western Thrace Basin, Greece and Bulgaria. J Sediment Res 82:482–498. doi:10.2110/jsr.2012.31

Ceriani S, Mancktelow NS, Pennacchioni G (2003) Analogue modelling of the influence of shape and particle/matrix interface lubrication on the rotational behaviour of rigid particles in simple shear. J Struct Geol 25:2005–2021. doi:10.1016/S0191-8141(03)00098-1

Clemens JD, Vielzeuf D (1987) Constraints on melting and magma production in the crust. Earth Planet Sci Lett 86:287–306

Coggon R, Holland TJB (2002) Mixing properties of phengitic micas and revised garnet-phengite thermobarometers. J Metamorph Geol 20:683–696. doi:10.1046/j.1525-1314.2002.00395.x

Collings D, Savov I, Maneiro K, Baxter E, Harvey J, Dimitrov I (2016) Late Cretaceous UHP metamorphism recorded in kyanite–garnet schists from the Central Rhodope Mountains, Bulgaria. Lithos 246–247:165–181. doi:10.1016/j.lithos.2016.01.002

Connolly JAD (2005) Computation of phase equilibria by linear programming: a tool for geodynamic modeling and its application to subduction zone decarbonation. Earth Planet Sci Lett 236:524–541. doi:10.1016/j.epsl.2005.04.033

Corfu F, Hanchar JM, Hoskin PWO, Kinny P (2003) Atlas of zircon textures. Rev Mineral Geochem 53:469–500. doi:10.2113/0530469

Cornelius N (2008) UHP metamorphic rocks of the Eastern Rhodope Massif, NE Greece: new constraints from petrology, geochemistry and zircon ages, Dissertation. Johannes Gutenberg-Universität Mainz, Mainz, Germany

Didier A, Bosse V, Cherneva Z, Gautier P, Georgieva M, Paquette JL, Gerdjikov I (2014) Syn-deformation fluid-assisted growth of monazite during renewed high-grade metamorphism in metapelites of the Central Rhodope (Bulgaria, Greece). Chem Geol 381:206–222. doi:10.1016/j.chemgeo.2014.05.020

Dinter DA, Royden L (1993) Late Cenozoic extension in northeastern Greece: Strymon Valley detachment system and Rhodope metamorphic core complex. Geology 21:45–48. doi:10.1130/0091-7613(1993)021<0045:LCEING>2.3.CO;2

Eisbacher GH (1970) Deformation Mechanics of Mylonitic Rocks and Fractured Granites in Cobequid Mountains, Nova Scotia, Canada. Geol Soc Am Bull 81:2009–2020. doi:10.1130/0016-7606(1970)81[2009:DMOMRA]2.0.CO;2

Escher A, Escher JC, Watterson J (1975) The Reorientation of the Kangâmiut Dike Swarm, West Greenland. Can J Earth Sci 12:158–173. doi:10.1139/e75-016

Forte AM, Bailey CM (2007) Testing the utility of the porphyroclast hyperbolic distribution method of kinematic vorticity analysis. J Struct Geol 29:983–1001. doi:10.1016/j.jsg.2007.01.006

Froitzheim N, Jahn-Awe S, Frei D, Wainwright AN, Mass R, Georgiev N, Nagel TJ, Pleuger J (2014) Age and composition of meta-ophiolite from the Rhodope Middle Allochthon (Satovcha, Bulgaria): A test for the maximum-allochthony hypothesis of the Hellenides. Tectonics 33:2014TC003526. doi:10.1002/2014TC003526

Fuhrman ML, Lindsley DH (1988) Ternary feldspar modeling and thermometry. Am Mineral 73:201–215

Ganguly J, Cheng W, Tirone M (1996) Thermodynamics of aluminosilicate garnet solid solution: new experimental data, an optimized model, and thermometric applications. Contrib Mineral Petrol 126:137–151. doi:10.1007/s004100050240

Gervilla F, Padrón-Navarta JA, Kerestedjian T, Sergeeva I, González-Jiménez JM, Fanlo I (2012) Formation of ferrian chromite in podiform chromitites from the Golyamo Kamenyane serpentinite, Eastern Rhodopes, SE Bulgaria: a two-stage process. Contrib Mineral Petrol 164:643–657. doi:10.1007/s00410-012-0763-3

Ghosh SK, Ramberg H (1976) Reorientation of inclusions by combination of pure shear and simple shear. Tectonophysics 34:1–70. doi:10.1016/0040-1951(76)90176-1

Goranov A, Atanasov G (1992) Lithostratigraphy and formation conditions of Maastrichtian-Paleocene deposits in Krumovgrad district. Geol Balc 22:71–82

Georgieva M, Bosse V, Cherneva Z, et al (2010) Late-Jurassic granulite facies metamorphism of garnet-bearing metabasic rocks from the Chepelare area, Central Rhodope. Bulgarian Geological Society, pp 31–32. http://www.bgd.bg/CONFERENCES/Geonauki_2010/Sbornik/pdf/10_Georgieva_GeoSciences_2010.pdf

Georgieva M, Bosse V, Cherneva Z, Kirilova M (2011) Products of HP melting in Chepelare shear zone, Central Rhodope, Bulgaria – petrology, P-T estimates and U-Th-Pb dating. Bulgarian Geological Society, pp 55–56. http://www.bgd.bg/CONFERENCES/Geonauki_2011/Sbornik/pdf/22_Georgieva_M.pdf

Harris NBW, Caddick M, Kosler J, Goswami S, Vance D, Tindle AG (2004) The pressure–temperature–time path of migmatites from the Sikkim Himalaya. J Metamorph Geol 22:249–264. doi:10.1111/j.1525-1314.2004.00511.x

Holland TJB, Powell R (1998) An internally consistent thermodynamic data set for phases of petrological interest. J Metamorph Geol 16:309–343. doi:10.1111/j.1525-1314.1998.00140.x

Holland TJB, Powell R (2001) Calculation of phase relations involving haplogranitic melts using an internally consistent thermodynamic dataset. J Petrol 42:673–683. doi:10.1093/petrology/42.4.673

Holland TJB, Baker J, Powell R (1998) Mixing properties and activity-composition relationships of chlorites in the system MgO–FeO–Al$_2$O$_3$–SiO$_2$–H$_2$O. Eur J Mineral 10:395–406

Hollister LS (1966) Garnet zoning: an interpretation based on the rayleigh fractionation model. Science 154:3757. doi:10.1126/science0.1647

Jahn-Awe S, Pleuger J, Frei D, Georgiev N, Froitzheim N, Nagel TJ (2012) Time constraints for low-angle shear zones in the Central Rhodopes (Bulgaria) and their significance for the exhumation of high-pressure rocks. Int J Earth Sci (Geol Rundsch) 101:1971–2004. doi:10.1007/s00531-012-0764-5

Jeffery GB (1922) The motion of ellipsoidal particles immersed in a viscous fluid. Proc R Soc Lond Ser A 102:161–179. doi:10.1098/rspa.1922.0078

Kirchenbaur M, Pleuger J, Jahn-Awe S, Nagel TJ, Froitzheim N, Fonseca ROC, Münker C (2012) Timing of high-pressure metamorphic events in the Bulgarian Rhodopes from Lu–Hf garnet geochronology. Contrib Miner Petrol 163:897–921. doi:10.1007/s00410-011-0705-5

Kounov A, Wüthrich E, Seward D, Burg J-P, Stockli D (2015) Low-temperature constraints on the Cenozoic thermal evolution of the Southern Rhodope Core Complex (Northern Greece). Int J Earth Sci (Geol Rundsch) 1–16. doi:10.1007/s00531-015-1158-2

Krenn K, Bauer C, Proyer A, Klötzli U, Hoinkes G (2010) Tectonometamorphic evolution of the Rhodope orogen. Tectonics 29:TC4001. doi:10.1029/2009TC002513

Krohe A, Mposkos E (2002) Multiple generations of extensional detachments in the Rhodope Mountains (northern Greece): evidence of episodic exhumation of high-pressure rocks. Geol Soc Lond Sp Publications 204:151–178. doi:10.1144/GSL.SP.2002.204.01.10

Kydonakis K, Gallagher K, Brun J-P, Jolivet M, Gueydan F, Kostopoulos D (2014) Upper Cretaceous exhumation of the western Rhodope Metamorphic Province (Chalkidiki Peninsula, northern Greece). Tectonics 33:2014TC003572. doi:10.1002/2014TC003572

Law RD, Searle MP, Simpson RL (2004) Strain, deformation temperatures and vorticity of flow at the top of the Greater Himalayan Slab, Everest Massif, Tibet. J Geol Soc 161:305–320. doi:10.1144/0016-764903-047

Li C, Jiang D (2011) A critique of vorticity analysis using rigid clasts. J Struct Geol 33:203–219. doi:10.1016/j.jsg.2010.09.001

Liati A, Mposkos E (1990) Evolution of the eclogites in the Rhodope Zone of northern Greece. Lithos 25:89–99. doi:10.1016/0024-4937(90)90008-O

Liati A, Seidel E (1996) Metamorphic evolution and geochemistry of kyanite eclogites in central Rhodope, northern Greece. Contrib Mineral Petrol 123:293–307. doi:10.1007/s004100050157

Liati A, Gebauer D, Wysoczanski R (2002) U–Pb SHRIMP-dating of zircon domains from UHP garnet-rich mafic rocks and late pegmatoids in the Rhodope zone (N Greece); evidence for Early Cretaceous crystallization and Late Cretaceous metamorphism. Chem Geol 184:281–299. doi:10.1016/S0009-2541(01)00367-9

Lister GS, Snoke AW (1984) S-C Mylonites. J Struct Geol 6:617–638. doi:10.1016/0191-8141(84)90001-4

Marchev P, Singer B, Andrew C, Hasson M, Morritz R, Bonev N (2003) Characteristics and preliminary 40Ar/39Ar and 87Sr/86 Sr data of the Upper Eocene sedimentary-hosted low-sulfidation gold deposits Ada Tepe and Rosino, SE Bulgaria: possible relation with core complex formation. In: Eliopoulos DG (ed) Mineral exploration and sustainable development, Proceedings of the 7th Biennial SGA Meeting Athens. Millpress Science Publishers, Greece, pp 1193–1196

Marchev P, Singer B, Jelev D, Hasson M, Moritz R, Bonev N (2004) The Ada Tepe deposit: a sediment-hosted, detachment fault-controlled, low-sulfidation gold deposit in the eastern Rhodopes, SE Bulgaria. Schweiz Miner Petrogr Mitt 84:59–78

Márton I, Moritz R, Spikings R (2010) Application of low-temperature thermochronology to hydrothermal ore deposits: formation, preservation and exhumation of epithermal gold systems from the Eastern Rhodopes, Bulgaria. Tectonophysics 483:240–254. doi:10.1016/j.tecto.2009.10.020

Moulas E, Kostopoulos D, Connolly JAD, Burg J-P (2013) P–T estimates and timing of the sapphirine-bearing metamorphic overprint in kyanite eclogites from Central Rhodope, northern Greece. Petrology 21:507–521. doi:10.1134/S0869591113050032

Mposkos ED, Kostopoulos DK (2001) Diamond, former coesite and supersilicic garnet in metasedimentary rocks from the Greek Rhodope: a new ultrahigh-pressure metamorphic province established. Earth Planet Sci Lett 192:497–506. doi:10.1016/S0012-821X(01)00478-2

Mposkos E, Liati A (1993) Metamorphic evolution of metapelites in the high-pressure terrane of the Rhodope Zone, northern Greece. Can Mineral 31:401–424

Mposkos E, Baziotis I, Leontakianakos G, Barry PH (2013) The metamorphic evolution of the high-pressure Kechros complex in East Rhodope (NE Greece): Implications from Na–Al-rich leucocratic rocks within antigorite serpentinites. Lithos 177:17–33. doi:10.1016/j.lithos.2013.06.012

Nagel TJ, Schmidt S, Janák M, Froitzheim N, Jahn-Awe S, Georgiev N (2011) The exposed base of a collapsing wedge: the Nestos Shear Zone (Rhodope Metamorphic Province, Greece). Tectonics 30:TC4009. doi:10.1029/2010TC002815

Newton RC, Charlu TV, Kleppa OJ (1980) Thermochemistry of the high structural state plagioclases. Geochim Cosmochim Acta 44:933–941. doi:10.1016/0016-7037(80)90283-5

Papadopoulos P (1982) Geologic map of Greece, Scale 1:50 000, Sheet Maronia, IGME Athens

Papanikolaou D, Panagopoulos A (1981) On the structural style of Southern Rhodope, Greece. Geol Balc 11:13–22.

Passchier CW (1987) Stable positions of rigid objects in non-coaxial flow—a study in vorticity analysis. J Struct Geol 9:679–690. doi:10.1016/0191-8141(87)90152-0

Perraki M, Proyer A, Mposkos E, Kaindl R, Hoinkes G (2006) Raman micro-spectroscopy on diamond, graphite and other carbon polymorphs from the ultrahigh-pressure metamorphic Kimi Complex of the Rhodope Metamorphic Province, NE Greece. Earth Planet Sci Lett 241:672–685. doi:10.1016/j.epsl.2005.11.014

Reischmann, T, Kostopoulos, D (2002) Timing of UHPM in metasediments from the Rhodope Massif, N Greece. Geochim Cosmochim Acta 66, Suppl. 1, A633

Ricou L-E, Burg J-P, Godfriaux I, Ivanov Z (1998) Rhodope and Vardar: the metamorphic and the olistostromic paired belts related to the Cretaceous subduction under Europe. Geodin Acta 11:285–309

Sarov S, Yordanov B, Georgiev S, Valkon V, Balkanska E, Grozdev V, Marinova R, Markov N (2007) Geological Map of Bulgaria, scale 1:50000, Map sheets K-35-88-V (Krumovgrad) and K-35-100-A (Egrek)

Schenker FL, Fellin MG, Burg J-P (2015) Polyphase evolution of Pelagonia (northern Greece) revealed by geological and fission-track data. Solid Earth 6:285–302. doi:10.5194/se-6-285-2015

Schmidt S, Nagel TJ, Froitzheim N (2010) A new occurrence of microdiamond-bearing metamorphic rocks, SW Rhodopes, Greece. Eur J Miner 22:189–198

Siivola J, Schmid R (2007) A systematic nomenclature for metamorphic rocks 12. List of mineral abbreviations. Recommendations by the IUGS Subcommission on the Systematics of Metamorphic Rocks. http://www.bgs.ac.uk/scmr/docs/papers/paper_12.pdf

Sokoutis D, Brun JP, Van Den Driessche J, Pavlides S (1993) A major Oligo-Miocene detachment in southern Rhodope controlling north Aegean extension. J Geol Soc 150:243–246. doi:10.1144/gsjgs.150.2.0243

Spear FS (1993) Metamorphic Phase Equilibria and Pressure-Temperature-Time Paths. Mineralogical Society of America, Washington

Tajčmanová L, Konopásek J, Schulmann K (2006) Thermal evolution of the orogenic lower crust during exhumation within a thickened Moldanubian root of the Variscan belt of Central Europe. J Metamorph Geol 24:119–134. doi:10.1111/j.1525-1314.2006.00629.x

Tajčmanová L, Connolly JAD, Cesare B (2009) A thermodynamic model for titanium and ferric iron solution in biotite. J Metamorph Geol 27:153–165. doi:10.1111/j.1525-1314.2009.00812.x

Teipel U, Eichhorn R, Loth G, Rohrmüller J, Höll R, Kennedy A (2004) U-Pb SHRIMP and Nd isotopic data from the western Bohemian Massif (Bayerischer Wald, Germany): implications for Upper Vendian and Lower Ordovician magmatism.

Int J Earth Sci (Geol Rundsch) 93:782–801. doi:10.1007/s00531-004-0419-2

Tracy RJ (1982) Compositional zoning and inclusions in metamorphic minerals. In: Ferry JM (ed) Characterisation of metamorphism through mineral equilibria. Mineralogical Society of America, Washington, pp 355–397

Turpaud P, Reischmann T (2010) Characterisation of igneous terranes by zircon dating: implications for UHP occurrences and suture identification in the Central Rhodope, northern Greece. Int J Earth Sci (Geol Rundsch) 99:567–591. doi:10.1007/s00531-008-0409-x

Wallis SR, Platt JP, Knott SD (1993) Recognition of syn-convergence extension in accretionary wedges with examples from the Calabrian Arc and the Eastern Alps. Am J Sci 293:463–494. doi:10.2475/ajs.293.5.463

Wawrzenitz N, Mposkos E (1997) First evidence for Lower Cretaceous HP/HT-Metamorphism in the Eastern Rhodope, North Aegean Region, North-East Greece. Eur J Miner 9:659–664

White RW, Powell R, Holland TJB, Worley BA (2000) The effect of TiO2 and Fe2O3 on metapelitic assemblages at greenschist and amphibolite facies conditions: mineral equilibria calculations in the system K2O–FeO–MgO–Al2O3–SiO2–H2O–TiO2–Fe2O3. J Metamorph Geol 18:497–511. doi:10.1046/j.1525-1314.2000.00269.x

White RW, Powell R, Holland TJB (2001) Calculation of partial melting equilibria in the system Na2O–CaO–K2O–FeO–MgO–Al2O3–SiO2–H2O (NCKFMASH). J Metamorph Geol 19:139–153. doi:10.1046/j.0263-4929.2000.00303.x

Wüthrich ED (2009) Low Temperature Thermochronology of the northern Aegean (Rhodope Massif), Dissertation. ETH Zürich, Zürich

Xypolias P (2010) Vorticity analysis in shear zones: A review of methods and applications. J Struct Geol 32:2072–2092. doi:10.1016/j.jsg.2010.08.009

Zagorchev I, Balica C, Balintoni I, Kozhoukharova E, Sabau G, Dimitrescu R, Negulescu E (2012) Isotopic data on the age of the Krupnik granite pluton and its host rocks Kresna horst, Krupnic mountain, SW Bulgaria. Comptes rendus de l'Academie bulgare des Sciences 65:977–984